AFRL-AFOSR-VA-TR-2020-0187

Injectable Mesh Nanoelectronics for Brain Mapping and Modulation

Adam Cohen
HARVARD COLLEGE PRESIDENT & FELLOWS OF

09/14/2020
Final Report

Air Force Research Laboratory
AF Office Of Scientific Research (AFOSR)/ RTB2
Arlington, Virginia 22203
Air Force Materiel Command

REPORT DOCUMENTATION PAGE

Form Approved
OMB No. 0704-0188

1. REPORT DATE *(DD-MM-YYYY)*	2. REPORT TYPE	3. DATES COVERED *(From - To)*
05-10-2020	Final Performance	01 Sep 2018 to 31 Aug 2020

4. TITLE AND SUBTITLE
Injectable Mesh Nanoelectronics for Brain Mapping and Modulation

5a. CONTRACT NUMBER

5b. GRANT NUMBER
FA9550-18-1-0469

5c. PROGRAM ELEMENT NUMBER
61102F

6. AUTHOR(S)
Adam Cohen

5d. PROJECT NUMBER

5e. TASK NUMBER

5f. WORK UNIT NUMBER

7. PERFORMING ORGANIZATION NAME(S) AND ADDRESS(ES)
HARVARD COLLEGE PRESIDENT & FELLOWS OF
1350 MASS AVE STE 600
CAMBRIDGE, MA 02138-3846 US

8. PERFORMING ORGANIZATION REPORT NUMBER

9. SPONSORING/MONITORING AGENCY NAME(S) AND ADDRESS(ES)
AF Office of Scientific Research
875 N. Randolph St. Room 3112
Arlington, VA 22203

10. SPONSOR/MONITOR'S ACRONYM(S)
AFRL/AFOSR RTB2

11. SPONSOR/MONITOR'S REPORT NUMBER(S)
AFRL-AFOSR-VA-TR-2020-0187

12. DISTRIBUTION/AVAILABILITY STATEMENT
A DISTRIBUTION UNLIMITED: PB Public Release

13. SUPPLEMENTARY NOTES

14. ABSTRACT

We have developed and exploited a new paradigm for electrical mapping and modulation of brain activity which we call syringe-injectable mesh electronics. Mesh electronics features tissue-like mechanical properties and connectivity and can be injected into and integrated with brain tissue with minimal invasiveness, enabling the unique capability to record from and stimulate the same neurons and neural circuits over long periods of time. In the first year of this project we advanced injectable mesh nanoelectronics capabilities for in-vivo studies, creating new silicon nanowire field-effect transistor (NWFET)-based mesh electronics, developed a strategy to protect the electronics against degradation in physiological environments, and initiating in-vivo physiological recording with this new tool, demonstrating for the first time multiplexed single-unit neuronal spike detection with the SiNW FET mesh, and highlighting its unique ability to record neuronal activities at subcellular resolution. Also, as a first step toward enable in-vivo neuron subtype electrophysiology, we functionalized mesh electronics with peptides and antibodies capable of targeting different cell types and achieved cell type-specific electrophysiological recording, selectively targeting neurons versus glia. Finally, we made a conceptual breakthrough in the design of 'neuron-like electronics' (NeuE) that enables unprecedented integration within the brain at the subcellular level, yielding an endogenous distribution of all major cell types as well as stable multiplexed single-unit recording of individual cells. The structure of NeuE appears to facilitate migration of endogenous neural progenitor cells, possibly due to its biomimetic neurite-like topographical features. We explored ways to further minimize the damage from implantation, and its ensuing immune response, by testing and optimizing injection

15. SUBJECT TERMS
nano FET, memory, electrical stimulation

16. SECURITY CLASSIFICATION OF:			17. LIMITATION OF ABSTRACT	18. NUMBER OF PAGES	19a. NAME OF RESPONSIBLE PERSON
a. REPORT	b. ABSTRACT	c. THIS PAGE			BRADSHAW, PATRICK
Unclassified	Unclassified	Unclassified	UU		19b. TELEPHONE NUMBER *(Include area code)* 703-588-8492

Standard Form 298 (Rev. 8/98)
Prescribed by ANSI Std. Z39.18

Final Performance Report – Years 1-2

Project Title:	Injectable Mesh Nanoelectronics for Brain Mapping and Modulation
Award Number:	FA9550-18-1-0469
Reporting Period:	9/01/2018 - 8/31/2020
Program Manager:	Dr. Patrick O. Bradshaw Mathematics, Information and Life Sciences Directorate Human Performance and Biosystems Air Force Office of Scientific Research 875 North Randolph Street 4027 Arlington, VA 22203 E-mail: Patrick.Bradshaw@afosr.af.mil Phone: (703) 588-8492
Principal Investigator:	Professor Adam E. Cohen Department of Chemistry and Chemical Biology Harvard University 12 Oxford Street Cambridge, MA 02138 E-mail: cohen@chemistry.harvard.edu Phone: (617) 496-9466

Final Technical Report - Years 1-2

Introduction. The broad aims of this project have been to develop and exploit a new paradigm for electrical mapping and modulation of brain activity which we call syringe-injectable mesh electronics. Our achievements during the first year of this project build upon our previous introduction of this fundamentally new technology, which features tissue-like mechanical properties and connectivity and can be injected into and integrated with brain tissue with minimal invasiveness, enabling the unique capability to record from and stimulate the same neurons and neural circuits over long periods of time. In the first year of this project we have made significant strides on Specific Aim 1: to advance current and develop new injectable mesh nanoelectronics capabilities for in-vivo studies. Specifically, we have **(1)** designed and fabricated new silicon nanowire field-effect transistor (NWFET)-based mesh electronics, developed a strategy to protect the electronics against degradation in physiological environments, and initiated in-vivo physiological recording with this new tool, demonstrating for the first time multiplexed single-unit neuronal spike detection with the SiNW FET mesh, and highlighting its unique ability to record neuronal activities at subcellular resolution. **(2)** We have functionalized mesh electronics with peptides and antibodies capable of targeting different cell types and achieved cell type-specific electrophysiological recording, selectively targeting neurons versus glia. Our successful efforts, evidenced by the natural distribution of both neurons and glial cells post-implantation, suggests that functionalizing mesh electronics with antibodies or aptamers capable of recognizing specific cell-surface receptors could enable in-vivo neuron subtype electrophysiology. **(3)** We have made a conceptual breakthrough in the design of bio-inspired mesh electronics, which we term 'neuron-like electronics' (NeuE), that provides unprecedented integration within the brain at the subcellular level, yielding an endogenous distribution of all major cell types as well as stable multiplexed single-unit recording of individual cells as early as two days post implantation. Moreover, the structure of NeuE appears to facilitate migration of endogenous neural progenitor cells, possibly due to its biomimetic neurite-like topographical features. **(4)** We have further minimized the damage, and ensuing immune response, caused during initial implantation by testing and optimizing injection parameters.

In Year 2 of the project, we have made significant progress on Specific Aim 2: to study the time-dependent evolution of neural circuits involved in defining the interplay between sensory input and cognitive performance in mice with an emphasis on spatial learning and memory. Specifically, we have demonstrated the ability to **(1)** use mesh electronics for spatial learning with single-neuron electrophysiological recording, **(2)** simultaneously record single-neuron electrophysiology across multiple brain regions involved in learning and memory tasks, **(3)** stably record from hundreds of neurons, and **(4)** record the evolution of spatial learning and memory over multiple months.

Note:

The original Principal Investigator on FA9550-18-1-0469, Professor Charles Lieber, was placed on administrative leave by Harvard University January 28, 2020. The award was transferred to Professor Adam Cohen with a revised termination date of August 31, 2020. Prof. Cohen supervised the ongoing research until the last personnel departed on August 22nd. The technical portion of this report for Year 2 describes research following an experimental design conceived by Prof. Lieber and carried out by Dr. Theodore Zwang, Dr. Tao Zhou and graduate student Jianxiang Qiu under Prof. Lieber's supervision until 1/28/20 and Prof. Cohen's supervision during the period 1/28/20-8/22/20. This report was drafted by Dr. Zwang and Dr. Kathleen Ledyard and reviewed, edited and approved by Professor Cohen.

YEAR 1

(1) Incorporation of silicon nanowire field-effect transistors (SiNW FET) into syringe-injectable mesh electronics.

We have previously reported the fabrication of ultra-flexible bioinspired metal-electrode-based mesh electronics. An important goal of this project has been to translate the advantages of nanoscale field-effect transistors – particularly their size and scalability – to our injectable mesh electronics.

Assembly, fabrication and electrical characterization of SiNW FET mesh networks. We have now developed photolithography protocols to successfully fabricate such SiNW FET mesh networks. As shown in **Fig. 1A**, the SiNW FET mesh networks are composed of I/O connects, interconnect stem and mesh parts. The photolithography process involves five major layers, as labelled in **Fig. 1B**: (i) a 350 nm SU8 top passivation layer, (ii) 1 nm/100 nm thermal-evaporated Cr/Au metal interconnects, (iii) a 350 nm SU8 bottom passivation layer, (iv) SU8 islands for supporting and assembling SiNWs, and (v) 50 nm thermal evaporated Au metal I/O connects for a 32-pin FFC interface. As described in our previous work, the SiNWs are assembled onto SU8 supporting islands through a direct contact printing method. The detailed schematic of a SiNW FET in **Fig. 1C** shows that the 2 μm wide Cr/Au contacts are fully encapsulated by 4 μm wide bottom and top SU8 passivation layers, where only the 2 μm SiNW channel is exposed as the sensing region. Prior to release from the wafer, the integrity of SiNW FET mesh networks is ascertained by optical microscope, as shown in **Fig. 1D**. SU8-encapsulated SiNW FETs can be treated as electrolyte-gated transistors when implanted in the mouse brain. **Fig. 1E** shows a linear conductance drop of 16 FETs from the same mesh when increasing gate voltage is applied on the grounding wire as the gate electrode, indicative of p-doping transport characteristics.

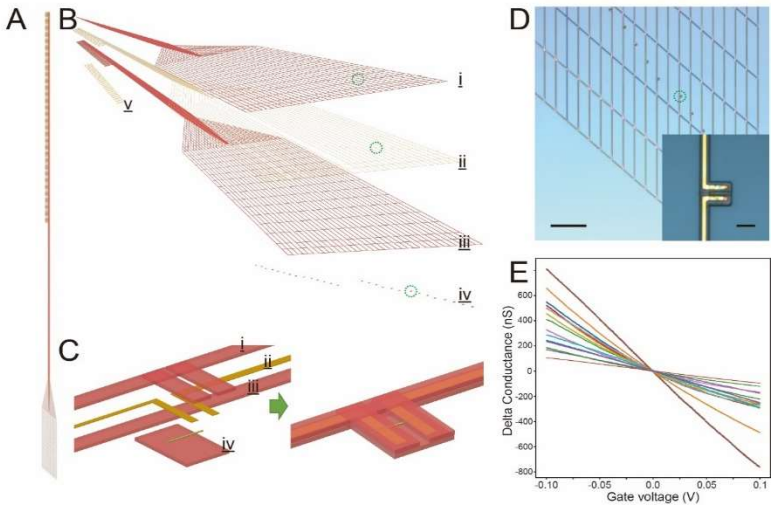

Figure 1. Fabrication and characterization of SiNW FET mesh networks. (A) The mesh is composed of 32-pin direct-contact input/output interface, interconnect stem and mesh containing 28 individually addressed SiNW FET nanodevices. **(B)** The SiNW FET mesh is fabricated by standard photolithography, consisting of five layers: i) top SU8 passivation, ii) metal contacts/interconnects, iii) bottom SU8 passivation, iv) SU8 supports for SiNWs and v) metal direct-contact input/output interface. **(C)** Detail of an individual SiNW FET nanodevice, labeled with green dashed circle in B. **(D)** Optical microscopic image of a fully fabricated SiNW FET mesh (scale bar 300 μm), with the inset showing an enlarged view of the green circle-labeled individual SiNW FET (scale bar 300 μm). **(E)** In-vivo SiNW FET conductance responses to electrolyte gate voltage applied through an implanted grounding electrode in the mouse brain.

Enhancement of SiNW FET mesh stability in physiological environments by ALD passivation. Previous studies have reported dissolution of nanoscale silicon under physiological conditions. Consequently the protection of SiNW FETs in mesh networks is a prerequisite for stable chronic recording in the mouse brain. Our group has previously demonstrated an ALD aluminum oxide passivation method to insulate on-chip SiNW FET from degradation in 1X phosphate buffered saline (PBS), extending its lifetime to at least 100 days. We have adopted this ALD passivation strategy in our fabrication. As shown in **Fig. 2A**, prior to SiNW assembly, a 5 nm ALD aluminum oxide layer was applied at 250°C, followed by rapid thermal annealing at 400°C for 1 min. As shown in **Fig. 2B**, the conductance of ALD-passivated SiNW decreases slowly, while an unpassivated SiNW FET survives less than eight days after implantation. In addition, **Fig. 2C** indicates the sensitivity of ALD passivated SiNW FET is stable and higher than 1000 V^{-1}; however, the majority of devices fail after 25 days post implantation. We are currently investigating several promising directions to further improve the stability of the SiNW FET devices, including (1) deposition of the aluminum oxide at higher temperatures and (2) higher temperature thermal annealing. Both of these approaches can improve the quality of the aluminum oxide and preliminary results indicate stability in excess of one month is readily achieved.

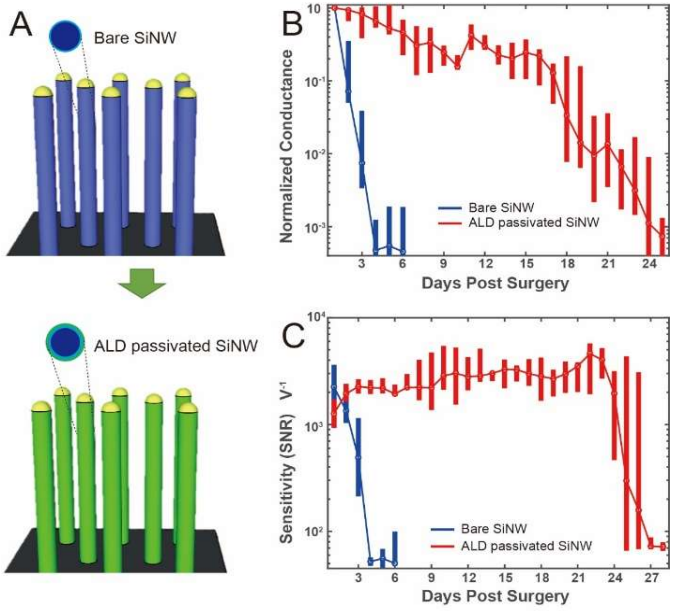

Figure 2. Improvement of SiNW FET durability through ALD aluminum oxide passivation. (A) Schematics of as-grown SiNW arrays before and after ALD aluminum oxide passivation. In-vivo device durability comparison of bare and 5 nm ALD aluminum oxide coated SiNW FET mesh nanoelectronics, after being implanted in mouse brain, in terms of normalized conductance **(B)** and device sensitivity **(C)**.

Single-unit neuronal spike detection on multiple SiNW FET channels. We have demonstrated for the first time multiplexed single-unit neuronal spike detection with SiNW FET mesh networks, highlighting its unique ability to record neuronal activities at subcellular resolution. In **Fig. 3A** the SiNW FET mesh is loaded into a glass capillary tube and precisely delivered into the hippocampal formation through the cortex by stereotaxic injection. In **Fig. 3B**, the implanted SiNW FET mesh forms a tubular structure. On Day 12 post implantation (**Fig. 3C**) single-unit neuronal spiking events are detected on four channels simultaneously. From the 250-5000 Hz bandpass filtered traces, these single-unit spikes exhibit large amplitude and signal-to-noise ratio, distinguishable from the submillivolt-level extracellular spike obtained by conventional metal microelectrode arrays. Applying wavelets and superparamagnetic clustering algorithm, the spikes can be clustered for further amplitude and waveform analysis (**Fig. 3D**). Notably, most spikes detected on the same SiNW FET channel have the same polarity, here shown as a single cluster in spike sorting, suggesting the device's capacity to record highly localized neuronal activities. In addition to the spikes on CH-0 presenting Gaussian distribution in amplitude and ca. 1 ms spike width, spikes

detected on CH-3 show a distinct heavy-tailed distribution and narrower spike width (ca. 0.5 ms), distinguishing the dendritic features from somatic spikes. To further examine the origin of these spikes, spiking activities were compared during awake and anesthetized recording. **Fig. 3E** shows that spike mean firing rates on both CH-0 and CH-3 were suppressed, from 0.83 Hz to 0.65 Hz and 1.32 Hz to 1.11 Hz, respectively. In addition, the spike amplitude on CH-0 slightly decreased upon anesthesia, while the spike amplitude on CH-3 was greatly suppressed, featuring possible somatic and dendritic spikes, respectively.

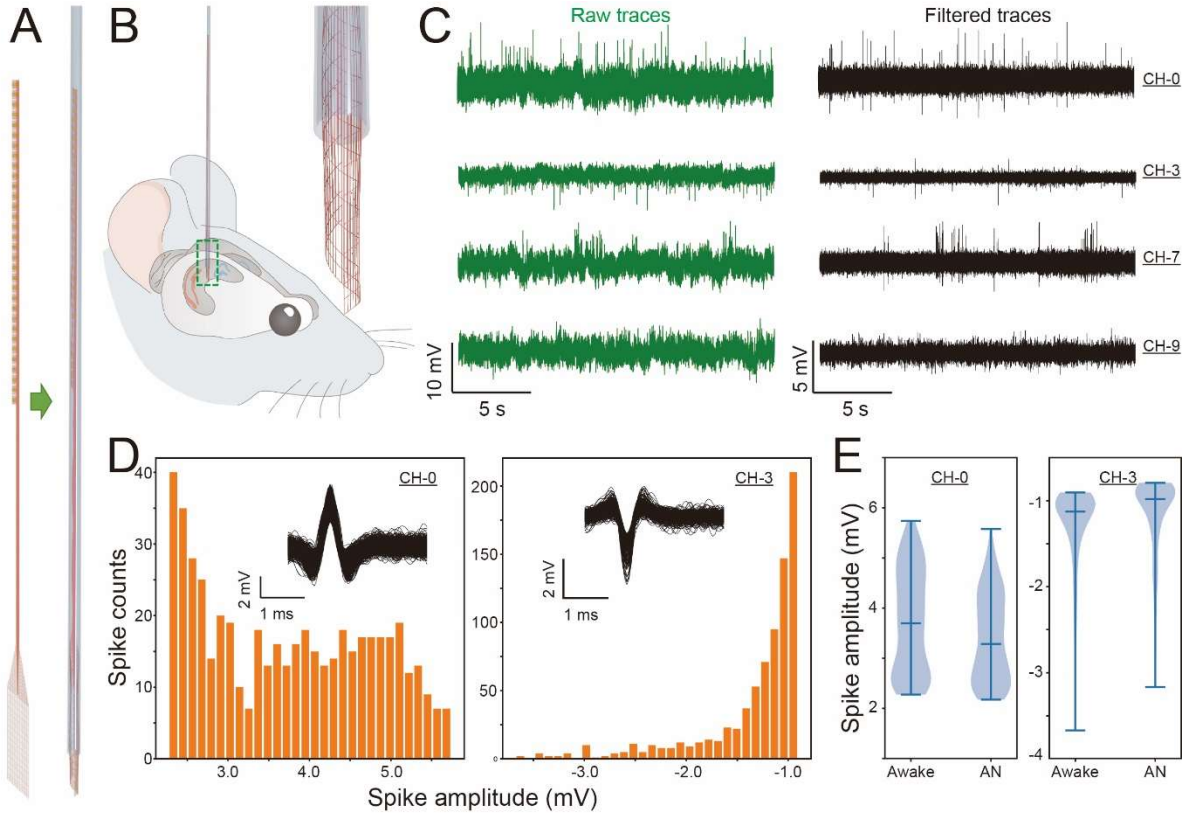

Figure 3. Multiplexed single-unit neuronal spike detection on SiNW FET channels. **(A)** SiNW FET mesh nanoelectronics loaded into glass capillary tube). **(B)** Implantation into mouse hippocampal formation and cortex. Inset: enlarged view of mesh nanoelectronics injection through a glass capillary. **(C)** Single-unit neuronal spike detection on 4 channels, with raw and filtered traces (250-5000 Hz bandpass filter) in green and black, respectively. **(D)** Sorted spike amplitude histograms of two types of spikes on channel-0 (CH-0) and channel-3 (CH-3), with insets showing the corresponding overlaid spike waveforms. **(E)** Violin charts of spike amplitude distribution on CH-0 and CH-3 in awake and anesthetized (AN) mice, showing anesthesia-regulated neuronal activities.

(2) Biochemical modification of mesh electronics.

The basic design of our mesh electronics has eliminated many of the structural and mechanical mismatches with brain tissue that are responsible for the chronic immune response elicited by conventional rigid neural probes. This thus represents a unique position from which to investigate elaboration of the mesh structure to exploit biochemical modification strategies for added functionality. To this end, we have carried out initial functionalization studies of the mesh electronics with peptides and antibodies capable of specific targeting of different cell types, with an emphasis on targeting neurons versus glial cells.

Functionalization of mesh electronics. To target and record from specific cell types using mesh electronics, we developed a surface modification approach for selective conjugation of peptides and antibodies on SU8 polymer ribbons (**Fig. 4**). First, we selected peptides and antibodies that can bind to specific cell surface receptors or the extracellular domain of membrane proteins. For

neurons, we used the peptide sequence Ile-Lys-Val-Ala-Val (IKVAV), an amino acid peptide fragment of the laminin α-1 chain in the extracellular matrix. For astrocytes, we chose antibodies targeting EAAT2, a membrane-targeted, Na^+-dependent glutamate transporter, which is highly expressed in mature astrocytes. For microglial cells, we chose antibodies targeting the microglia surface marker CD11b. To exclude the possible effects of immune response (i.e., accumulation of astrocytes and microglial cells) induced by foreign antibodies, we also included a rabbit anti-human IgG antibody as control antibody that does not bind to cells in the mouse brain. Second, the -NH_2 groups on peptides and primary antibodies were covalently coupled to the carboxyl (-COOH) groups on oxygen plasma-treated SU8 polymer using 1-ethyl-3-(3-(dimethylamino)propyl) carbodiimide (EDC) and N-hydroxysuccinimide (NHS). The modification layer was characterized by incubating the mesh electronics in peptides or secondary antibodies labeled with fluorophores and then imaging the modified mesh using confocal fluorescence microscopy. Increased fluorescence on the SU8 ribbons signaled that these cases the respective peptides or antibodies were selectively conjugated onto SU8.

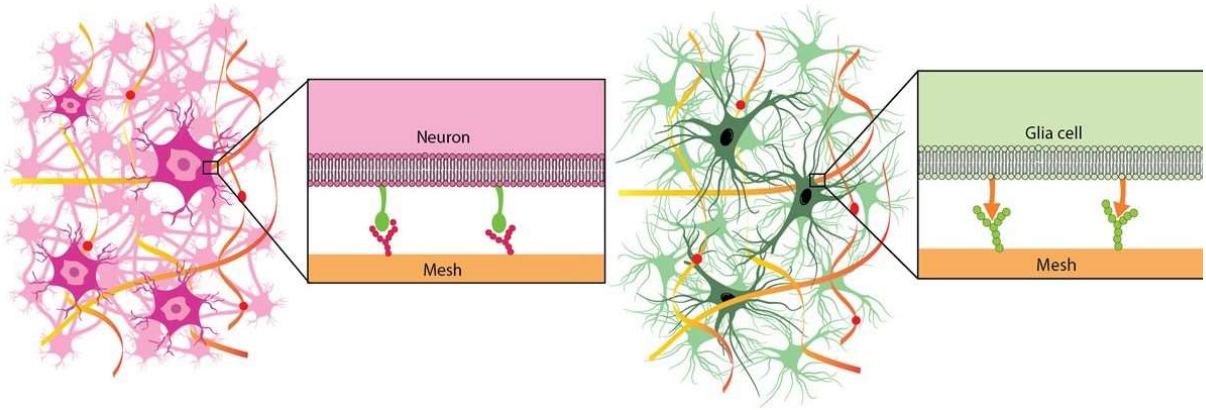

Figure 4. Functionalization of the mesh electronics. Schematics of mesh electronics conjugated with antibodies or aptamers capable of recognizing and targeting specific cell surface receptors attracting targeted neurons versus glia cells for specific cell type recording.

Cell type-specific electrophysiological recording. Following surface functionalization, modified and control mesh electronics were implanted into the hippocampal region of mouse brains for in-vivo chronic electrophysiological recording. Multiplexed recordings (**Fig. 5A**) exhibit stable single-unit spikes from the time of initial implantation to the endpoint of the measurements (two weeks). The number of distinct neurons recorded per electrode two weeks post injection from meshes with different modification (**Fig. 5B**) varies significantly. The neuron-targeting IKVAV peptide increased the number of recorded neurons, while the microglia-targeting anti-CD11b and astrocyte-targeting anti-EAAT2 antibodies significantly decreased the number of recorded neurons. In addition, control antibody-modified meshes recorded a similar number of neurons as the unmodified meshes, indicating that the modified meshes targeting specific cell types affect the natural distribution of neurons and glial cells without inducing immune response. The percentage distribution of average spike amplitude of distinct neurons and the average amplitude of the top 20% largest average spikes recorded from different meshes (**Fig. 5C,D**) further confirms that the IKVAV peptide can enhance neuron adhesion, while the accumulation of microglial cells and astrocytes reduced the number of neurons adjacent to the meshes.

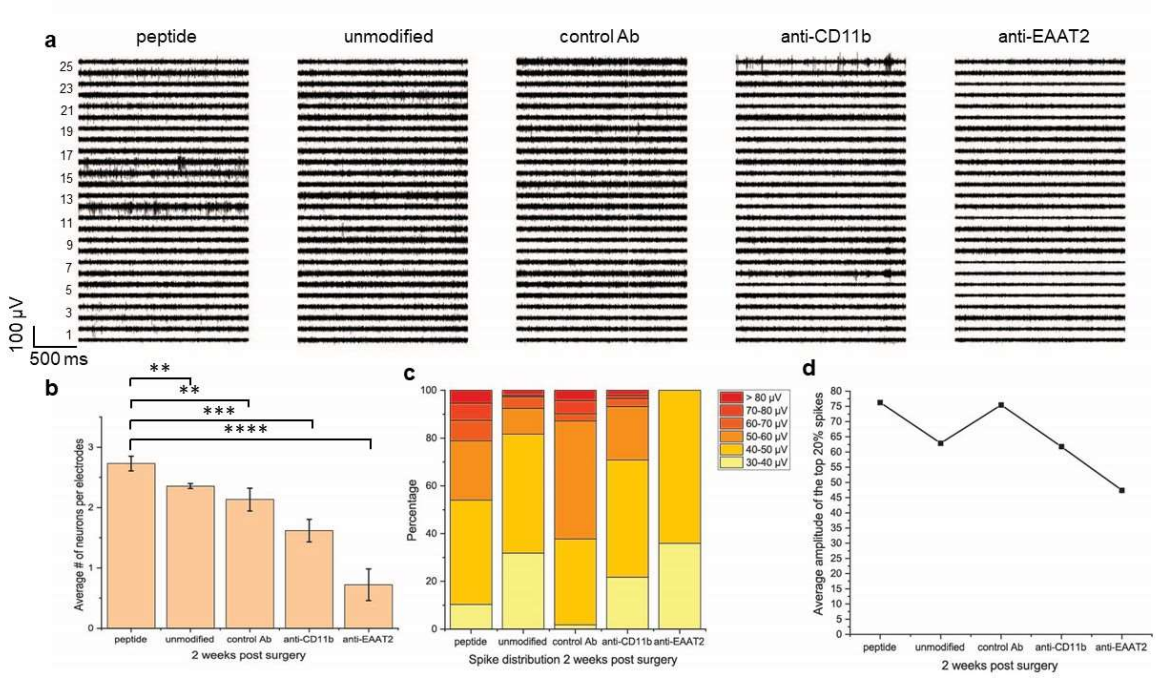

Figure 5. Cell type-specific electrophysiological recording. **(A)** Representative 26-channel single-unit spike traces two weeks post-injection from differently modified meshes. x and y axes represent recording time and voltage. **(B)** The number of distinct neurons recorded per electrode two weeks post injection. Statistical significances were obtained by comparing the datasets below the ends of the black line using Student's t-test. **P< 0.01, ***P<0.001, ****P< 0.0001. **(C)** Percentage distribution of average spike amplitude of distinct neurons recorded from different meshes. **(D)** Average amplitude of the top 20% largest average spikes from **(C)**.

Time-dependent histology studies of meshes targeting different cell types. To confirm the cell-targeting capabilities of our modified meshes, the distribution of microglial cells and astrocytes were compared in time-dependent histology studies (**Fig. 6**). Fluorescence images showed that microglial cells and astrocytes were specifically attracted to meshes modified with anti-CD11b and anti-EAAT2, respectively, as early as three days post implantation. Previous studies showed that the immune response (i.e., accumulation of microglia and astrocytes) induced by implanted electrodes peaks at day 3 and slowly disappears by one week. The accumulation of targeted cells two weeks post implantation confirms that the change in cell distribution is due to affinity for the modified antibodies rather than to immune response.

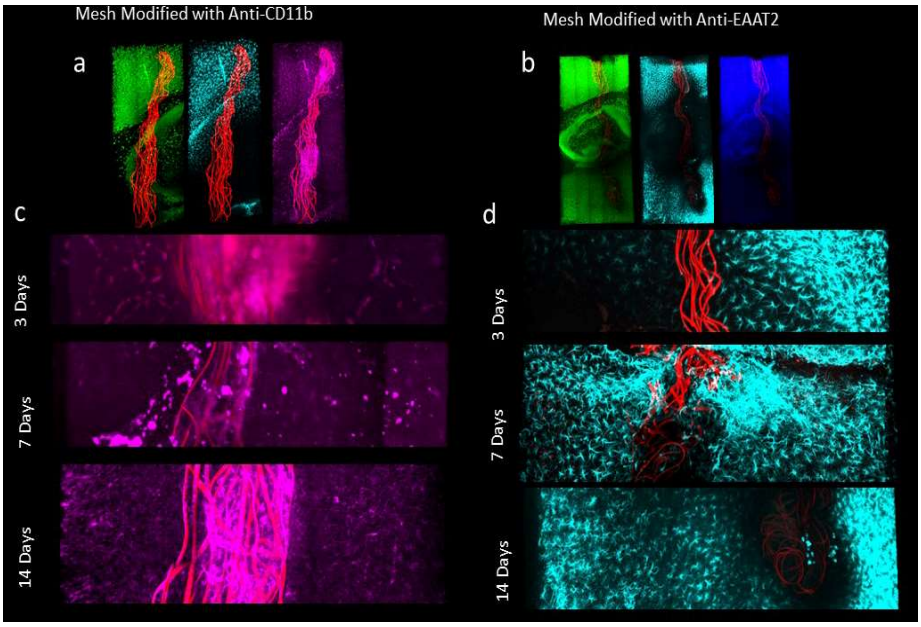

Figure 6. Mesh modified to specifically bind astrocytes or microglia. **(A)** Mesh modified with anti-CD11b to attract microglia was labeled with NeuN (green), GFAP (cyan), and Iba1 (magenta) 14 days after implantation. **(B)** Mesh modified with anti-EAAT2 to attract astrocytes was labeled with NeuN (green), GFAP (cyan), and DAPI (blue) 14 days after implantation. **(C)** Change in Iba1 labelling of microglia attracted to anti-CD11b mesh over time. **(D)** Change in GFAP labelling of astrocytes attracted to anti-EAAT2 mesh over time.

To further exclude the possible effects of immune response induced by foreign antibodies, time-dependent histology studies of unmodified meshes and meshes modified with control antibody and IKVAV peptide were carried out (**Fig. 7**). In meshes with control antibody or IKVAV peptide the distribution of neurons, astrocytes, or microglia is not significantly different from that adjacent to an unmodified mesh, further confirming that the modified meshes affect cell distribution without inducing an immune response.

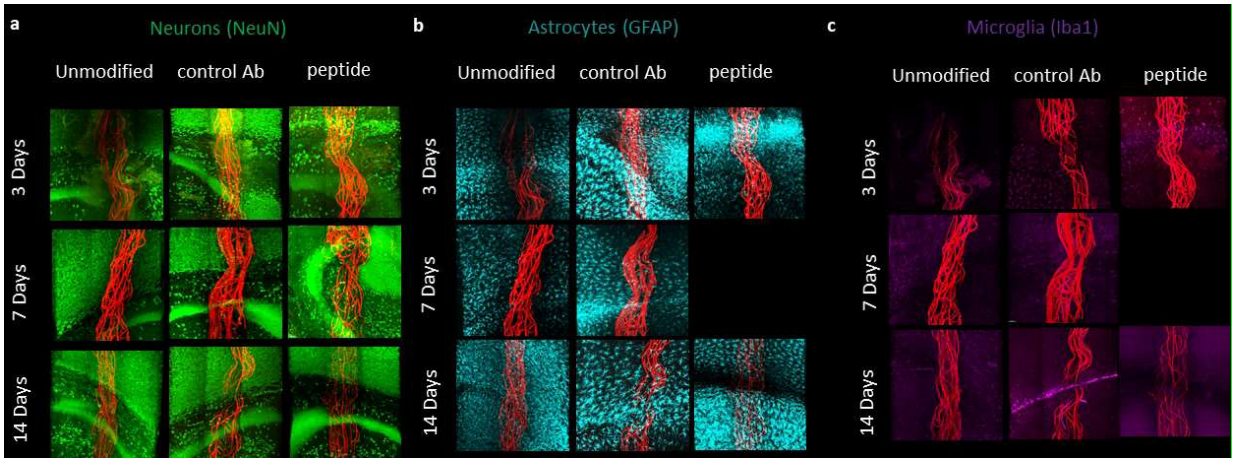

Figure 7. Modification of the mesh with nonspecific antibody and peptide. Fluorescence images of antibody labelled **(A)** neurons, **(B)** astrocytes, and **(C)** microglia. Modification of the mesh with control antibody or IKVAV peptide does not significantly change the distribution of neurons, astrocytes, or microglia compared to an unmodified mesh.

In summary, we have been able to achieve cell type-specific electrophysiological recording with mesh electronics functionalized with specific peptides and antibodies, and confirmed by time-

dependent histology studies that the cell distributions are attributable to mesh modification. Developing the cell-targeting capabilities of mesh electronics opens up new opportunities previously not possible for electrophysiology tools. For example, efforts to modify mesh electronics with antibodies that target neuron subtypes (e.g., dopaminergic neurons) are an obvious next step.

(3) Neuron-like electronics (NeuE): improved integration of flexible mesh electronics with neural networks through size reduction and increased flexibility.

To advance the current capabilities of injectable mesh electronics, we have dramatically decreased both its size and rigidity to create what we term neuron-like electronics (NeuE), which shows an enhanced ability to integrate seamlessly with brain tissue as well as to act as a scaffold to attract and interact with new neurons. These bioinspired neural probes were designed and fabricated to have key building blocks on the scale of subcellular structural features and mechanical properties comparable to those of neurons (**Fig. 8**). 3D mapping of implanted NeuE-brain interfaces reveals the structural indistinguishability of Neu E and neurons (**Fig. 8B,C**). Time-dependent histology studies on 3D tissue volumes from distinct brain regions reveal structurally stable and seamless interpenetrating interfaces with the neuronal networks shortly after implantation. Quantitative analysis of astrocyte and microglia distributions demonstrates that NeuE probes elicit negligible immune response in the brain from Day 2 post implantation onward. Importantly, NeuE probes demonstrate multiplexed stable single-unit recording of individual cells with stable signal-to-noise ratios in the nearly native physiological context without loss in recording quality from shortly after implantation to at least three months, attesting to a functionally stable interface with neuronal networks (**Fig. 8D,E**).

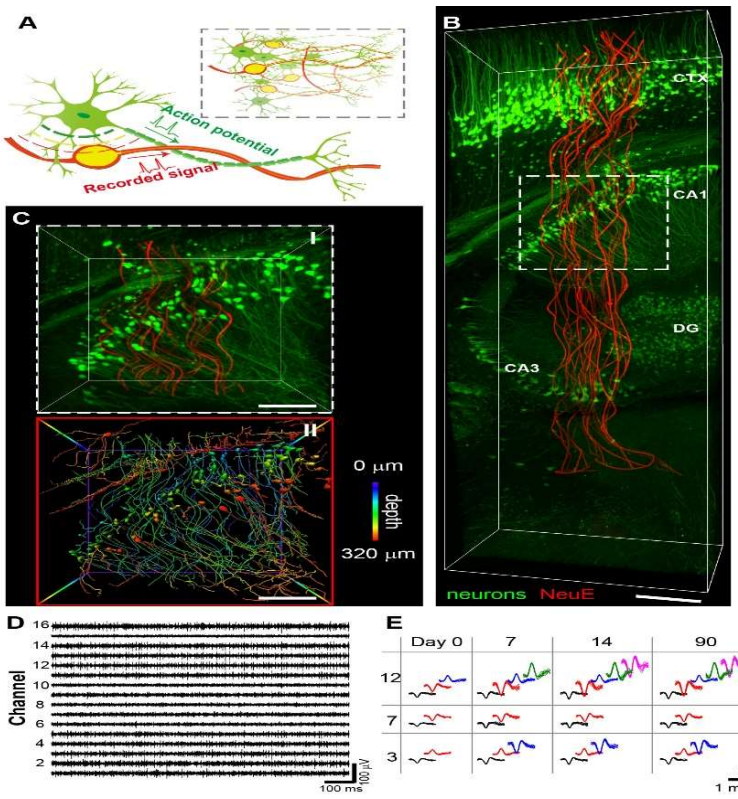

Figure 8. NeuE exhibits a seamlessly integrated and stable interface with the brain. (A) Schematics showing the structural similarity between NeuE and neurons from the subcellular level to the network level (inset). Neurons, green; electrodes and interconnects, yellow; polymer layers, red. **(B)** 3D reconstructed interface between neurons (green) and NeuE (red) six weeks post-implantation. Scale bar, 200 µm. **(C)** Enlargements of the white dashed box in B. I and II correspond to standard fluorescence and depth-coded images, respectively. Scale bars, 100 µm. **(D)** 16-channel single-unit spike traces seven days post injection. **(E)** Time evolution of spikes of principal component analysis clustered single units from three representative channels over three months post-injection.

Notably, the NeuE subcellular structural features are shown to facilitate migration of endogenous neural progenitor cells. There are substantial DCX^+ cells associated and aligned with the neurite-like NeuE structure, yet little or no DCX staining of $DAPI^+$ cells further away from the probe, as

shown in **Fig. 9A,B**. In addition, NeuE shows an approximately threefold increase ($P < 0.001$) in DCX^+ cells compared to the 20 μm control mesh at both one and two weeks post implantation (**Fig. 9C**), suggesting that the biomimetic neurite-like topographical features of NeuE may modulate endogenous cell behavior, including adhesion and migration.

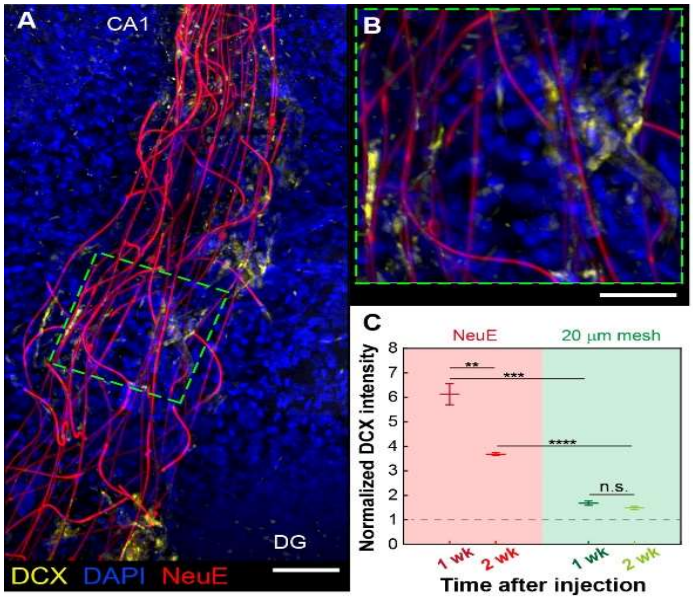

Figure 9. NeuE facilitates migration of newborn neurons. (A) 3D image showing the distribution of DCX^+ newborn neurons along NeuE one week post implantation. Yellow, blue and red colors represent DCX, DAPI and NeuE, respectively. Scale bar, 100 μm. **(B)** Magnified view of the green dashed box in A. Scale bar, 50 μm. **(C)** Normalized DCX intensity at 0–20 μm near the NeuE or 20 μm mesh normalized against baseline values remote to the probe (grey dashed horizontal line). All error bars reflect ±1 s.e.m.

(4) Optimization of mesh insertion procedure to minimize implantation footprint.

In our further development of mesh electronics, we have also considered the role played by injection parameters, which directly affect immune response to the implanted electronics. Because the high flexibility of the electronics precludes direct insertion, to date we have used syringe injection to implant the probes into tissue. However, the relatively large 400 μm inner diameter (ID)/550 μm to 650 μm outer diameter (OD) glass needles required for probe extrusion can acutely disturb the local tissue. To this end, we carried out systematic studies on new 2D and 1D mesh electronics designs that allow syringe injection via 100 μm ID glass needles with reduced saline volume.

Using finite element analysis, we rationally modulated the unit cell parameters of 2D mesh electronics to allow loading of and ejection from at least 4-fold reduced ID glass needles (**Fig. 10A**). Systematic in-vitro testing confirmed that the new mesh electronics designs injected via reduced-diameter needles require much reduced saline solution injection volumes compared to prior studies, enabling a significantly minimized injection footprint.

We also developed 1D designs, which have no transverse elements in the injected portion of the probe. The loading and injection characteristics of the 1D probes were roughly identical to their 2D analogues; but acute post-injection behavior in the injected media showed key differences. Micro-CT analysis of acute mouse brain injections was performed to assess the volume occupied by mesh electronics by 2D versus 1D designs as a function of needle size. First, for both designs, we found that the use of reduced-diameter needles resulted in probe cross-sectional diameters not statistically significantly different from those observed with standard needle sizes. Second, the similarity in mesh cross-sectional diameter across the needle sizes tested suggests that reducing needle diameter minimizes tissue damage while still allowing interaction with roughly the same volume of tissue accessed by larger needles. Last, removal of the transverse probe elements to

yield 1D mesh results in statistically significant probe compression relative to the 2D designs across different needle diameters (**Fig. 10B**).

Based on these results, we conclude that larger needles may result in increased tissue compression of the probe as the needle is retracted and that the presence of transverse elements is necessary to

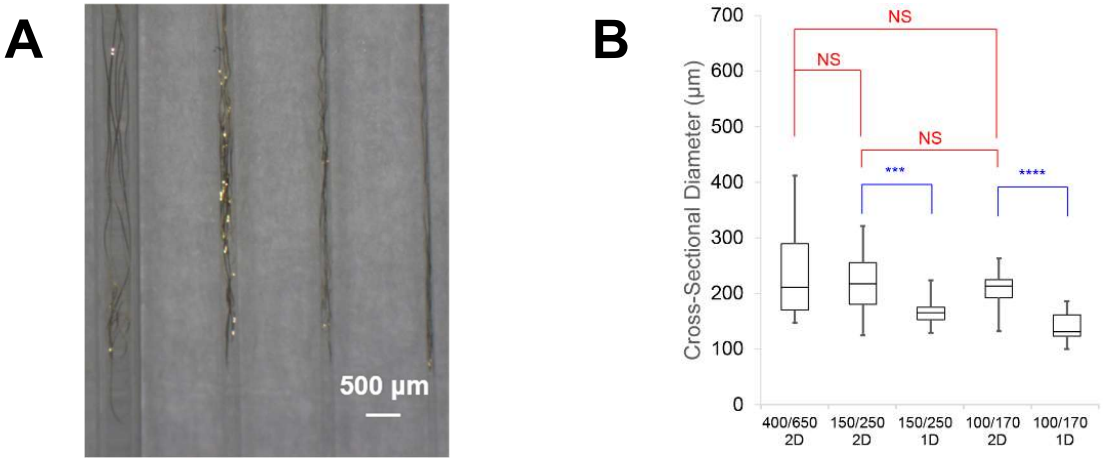

Fig. 10. **Minimization of injection footprint**. **(A)** Photographs of mesh electronics loaded in 400/650, 200/330, 150/250, and 100/170 µm ID/µm OD glass needles (left to right). **(B)** Cross-sectional diameters of acute mouse brain-injected mesh electronics using different needle sizes and mesh electronics designs. The red and blue indicate P values for 2D vs 2D and 2D vs 1D measurements, respectively, where NS (not significant) indicates $P > 0.05$, two asterisks indicate $P < 0.01$, three asterisks indicate $P < 0.001$, and four asterisks indicate $P < 0.0001$ (by a two-tailed t test).

provide a minimum transverse bending stiffness to circumvent strong probe compression from tissue relaxation. Consequently we have rationally designed mesh electronics with a significantly minimized implantation footprint, which we believe enables new opportunities in probe interfacing with tissue volume better matched to the needle-perturbed volume.

YEAR 2

(1) Use of mesh electronics to track spatial memory with single-neuron electrophysiological recording.

A major challenge in studying memory processes is that they occur over lengthy time scales and across multiple brain regions, yet they involve changes in individual neurons with millisecond activity. Previous longitudinal studies have typically used technology such as functional magnetic resonance imaging (fMRI), which allows for noninvasive probing of brain activity but lacks the spatiotemporal resolution to track changes in individual neurons over long periods of time. While electrophysiology probes can achieve single-neuron resolution and have been used in behavioral tasks, but they are typically unable to reliably record from the same neurons for periods longer than a few days or weeks due to local tissue damage. Microdrives must be used to change the position of probes to sample new neurons whenever recording from the previous area becomes impossible. Optical imaging of neural activity using fluorescent indicators allows for simultaneous recording of hundreds of neurons, but is limited by penetration depth and the requirement for implanted cranial windows, which can lead to fibrosis and imaging instability. While these technologies have made possible vital advances in our understanding of neuroscience, they do not have the properties necessary to track aging-related changes in single neurons and their circuits.

An important goal of this project has been to harness the advantages of mesh electronics, particularly their ability to record from single neurons over an extended period of time, to study

the time-dependent evolution of neural circuits involved in spatial learning and memory. To this end, we have built a virtual reality system that enables simultaneous electrophysiological recording and behavioral testing, allowing us to observe place cells within the hippocampus of C57BL/6J mice as they navigate along a virtual linear track.

Virtual reality system set-up. We built and programmed a virtual reality system for behavioral testing that has previously been used to study spatial memory in mice (**Fig. 11**). The virtual reality system was programmed in MATLAB using ViRMEn. A laser projector back-projected the virtual environment onto a half-cylindrical screen that fills the field of view of a head-fixed mouse. The mouse runs on a Styrofoam ball that is frictionless, suspended by a constant flow of air, and optical sensors under the ball are used to update the virtual environment in response to the mouse's locomotion.

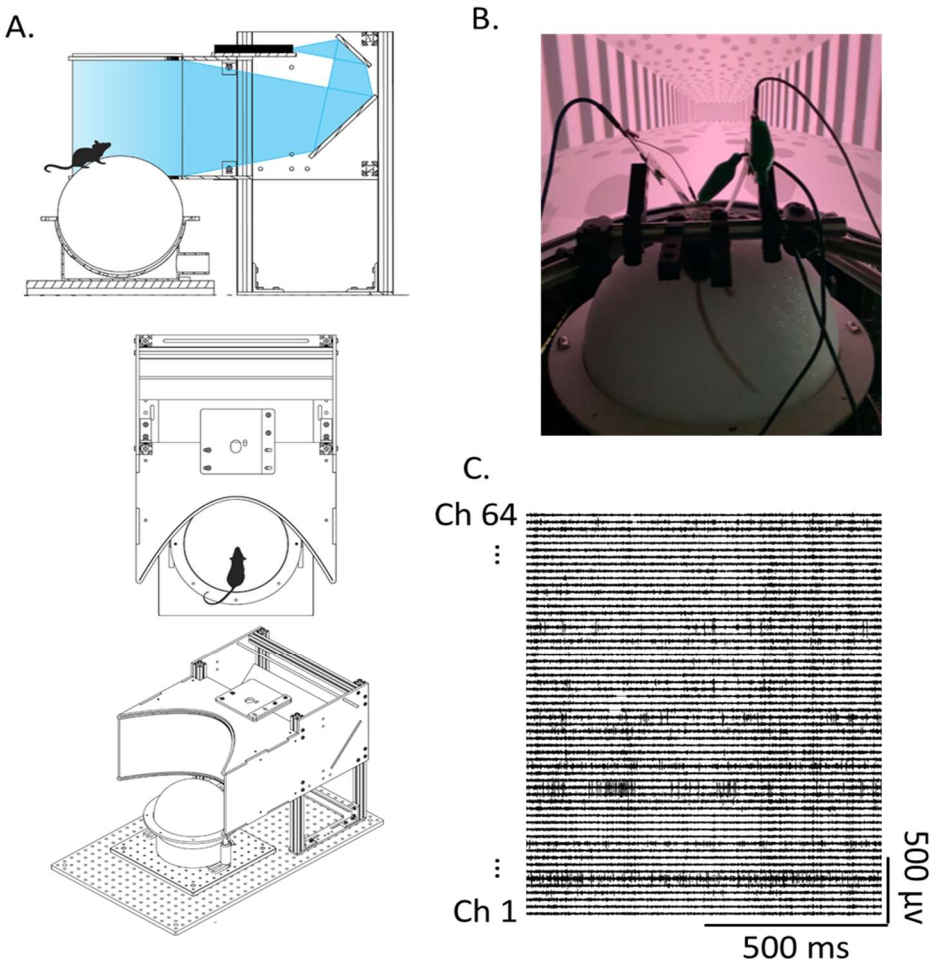

Figure 11. Virtual reality system for electrophysiology in behaving mice. (A) Basic schematic of the virtual reality system. A laser projector back-projected the virtual environment onto a half-cylindrical screen that fills the field of view of a head-fixed mouse. The mouse runs on a Styrofoam ball that is frictionless suspended by a constant flow of air, and optical sensors under the ball are used to update the virtual environment in response to the mouse's locomotion. (B) Image of the virtual reality system in operation. (C) Example of electrophysiology data collected via mesh electronics while the mouse is running on the virtual track.

Before behavioral training, two mesh electronics containing 32 electrodes each were implanted using a stereotaxic stage that allows for delivery to the following brain coordinates: Anteroposterior, -2.30 mm; Mediolateral, 1.75 mm:, and Dorsoventral, 2.5 mm in each hemisphere. Electrodes were distributed along the mesh such that they span the CA1, DG, and

CA3 regions of the hippocampus after implantation. On average 57/64 recording electrodes were connected after implantation and remained connected throughout the entire test period of 3 months. Spike clustering software, Wave_clus, was used to distinguish individual neurons and found an average of 236 separable clusters per mouse.

Mice were then trained to run along a 2-meter virtual track with water rewards given at random locations. Upon reaching the end of the virtual track, the mice were virtually teleported to the start so they would run through the same path multiple times within each 30-minute session. Electrophysiology was recorded, then processed, to isolate the firing frequency of each neuron at different positions along the virtual track. Approximately 35% of recording electrodes showed location-dependent increases in firing rates characteristic of place cells. A representative example of an individual place cell and non-place cell from the same recording electrode is shown in **Fig. 12.**

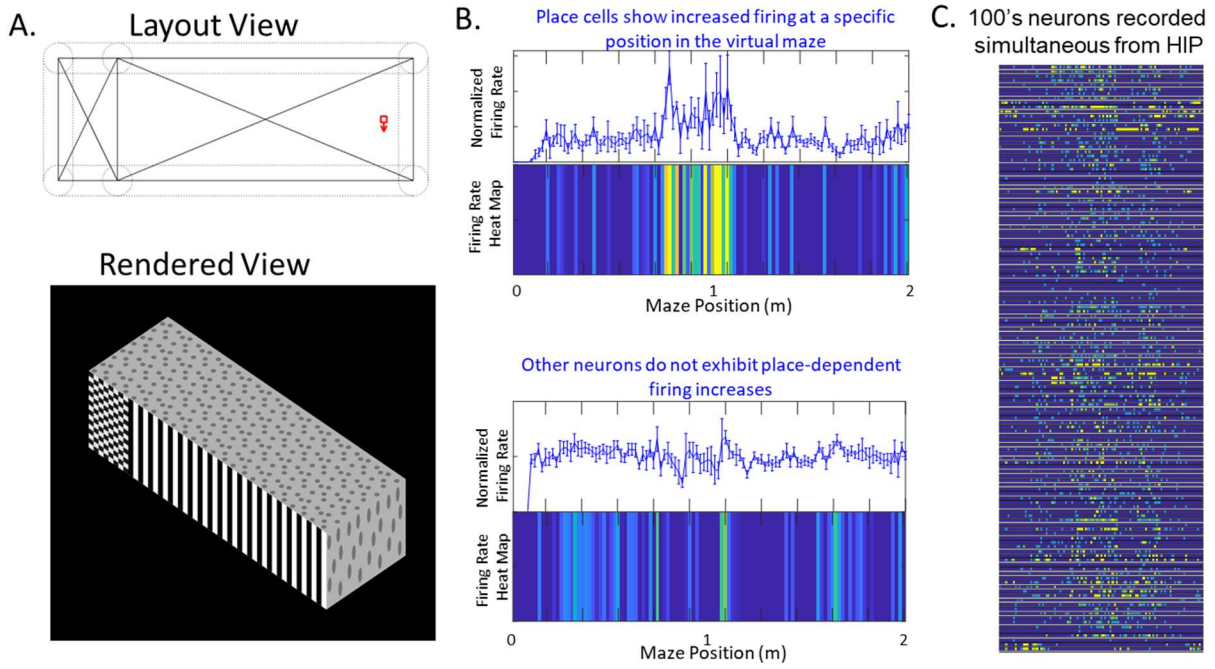

Figure 12. Measurement of place cells along a virtual track. (A) A simple linear track with vertical lined walls, spotted floor and ceiling, and checkered end was used to test the ability for mesh electronics to record place cells. Once the mouse reached the checkered region the screen would shut off for 2 seconds and the mouse would be teleported to the red icon at the start of the linear track. (B) Increased firing rates at specific positions along the track, indicative of place cells, were found for 35% of isolated neurons. (C) 100s of neurons were recorded simultaneously from the hippocampus; spatially resolved firing data from 100 separated clusters are shown each in their own row.

(2) Using mesh electronics to track the stability of place fields over time.

The hippocampus is among the best-studied regions of the brain with respect to memory. Many characteristics of hippocampal neural activity have been related to memory, such as the ability for place cells to be remembered when a mouse is repeatedly studied in the same environment. However, more dynamic properties of place cells have been found to show distinct changes with age, which is difficult to study in a single cell using conventional electronics that cannot interrogate the same cells for extended periods of time. There is evidence that there are differences in place map retrieval, spontaneous remapping of place fields stable environments, remapping of place fields to new environments, and spatial accuracy of learned locations.

Using mesh electronics, we recorded from the same individual neurons while mice traversed the same virtual track over the course of multiple months. As shown in **Fig. 13**, the place field for an

individual neuron was somewhat stable in position from week 16 to 25. However, changing the environment slightly in week 24 caused the place field to change, indicating that the mouse could tell it was in a different virtual environment. Returning the mouse to the original environment in week 25 showed the individual neuron could remember its place field.

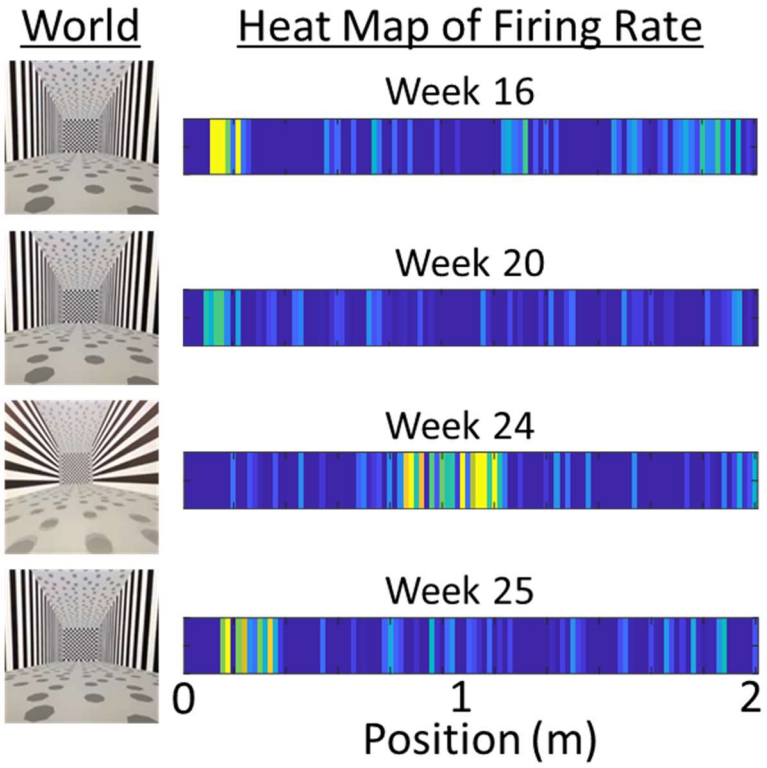

Figure 13. Stability and remapping of a single-neuron place field in virtual reality. A stable place field was observed over two months in the same environment. Changing the pattern on the walls caused the place cell to remap. Upon returning to the original environment, the place cell remembered its original firing field.

(3) Using mesh electronics to understand changes in circuitry with goal-oriented learning.

We trained mice in a goal-oriented learning task developed in the lab of Attila Losonczy for use with head-fixed mice in virtual reality. This task tracks place cell dynamics over a multiday learning task and can be used to track place cell remapping and a correlation between place cell map stability and learning performance in both wild-type and a disease model mouse with cognitive deficits. C57Bl/6J mice have been successfully used in other virtual reality tasks up to 27 months, and show stable visual acuity at 18 months of age, with a measurable decline starting after 23 months of age, which suggests they will be visually engaged and able to participate in the long-term tracking of goal-oriented learning task in virtual reality. The virtual maze shown in **Fig. 14** was used for trials of this task.

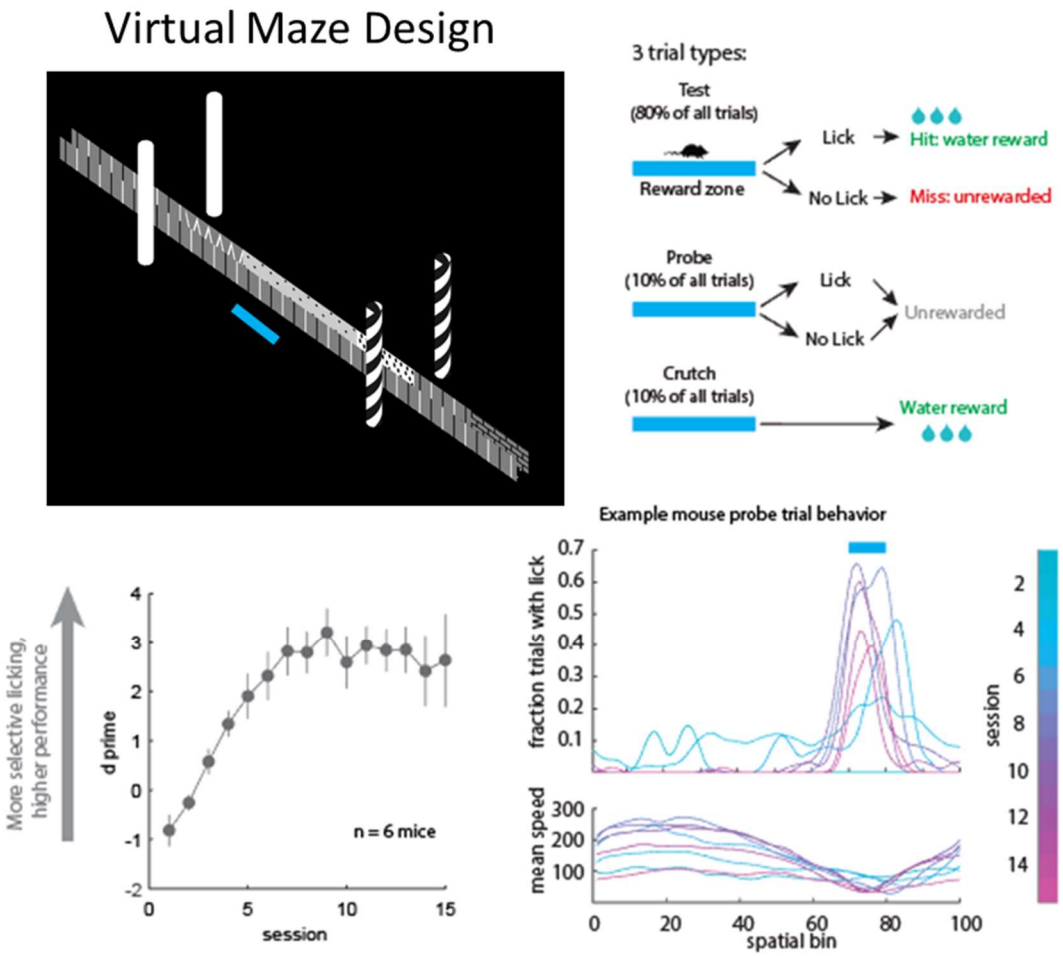

Figure 14. Goal-oriented learning task. (Top left) Design of virtual maze with more visual features. Blue line indicates the location of the reward zone. (Top right) Every time the mouse reaches the end of the track it is warped to the start and a trial type is randomly selected. (Bottom) As each mouse repeats this task in sessions on subsequent days they start to selectively lick in the reward position. These data indicate the mice are learning the location of the reward.

In this goal-oriented learning task, mice learn the location of a hidden 10-cm reward zone on a treadmill. During pre-training, the reward zones are shuffled each lap, which has the effect of training the mice to run and lick simultaneously, as the animals have no way of predicting the reward. Following pre-training, mice are placed in a novel context, and a single, fixed, uncued 10-cm reward zone is defined. 30-minute recording sessions take place every other day, allowing the mice to learn and remember the position of the hidden reward zone. Each recording session contains 80% test trials, 10% probe trials, and 10% crutch trials that are randomly assigned every time the mouse is teleported to the start of the maze. Mature adult C57Bl/6J mice reach their performance peak after seven sessions (**Fig. 14**). Task performance is assessed by monitoring the spatial distribution of licks. As the mice learn the task, they suppress their licking outside the reward zone and develop an anticipatory lick signal prior to reward zone entry. This results in a progressive increase in the fraction of licks occurring in the reward zone and provides a measurable behavioral expression of learning and memory.

Additionally, mice trained in this task were implanted with mesh electronics in both the entorhinal cortex and the hippocampus. Mesh was implanted into the entorhinal cortex using the following coordinates: Anteroposterior, -4.70 mm; Mediolateral, +/-2.55 mm; and Dorsoventral, 1.50-3.50 mm. As shown in **Fig. 15**, the place-dependent firing shows a different pattern than data collected

in the hippocampus (**Fig. 12C**). Some of these show firing patterns suggestive of border cells and grid cells; however further analysis is needed to confirm this.

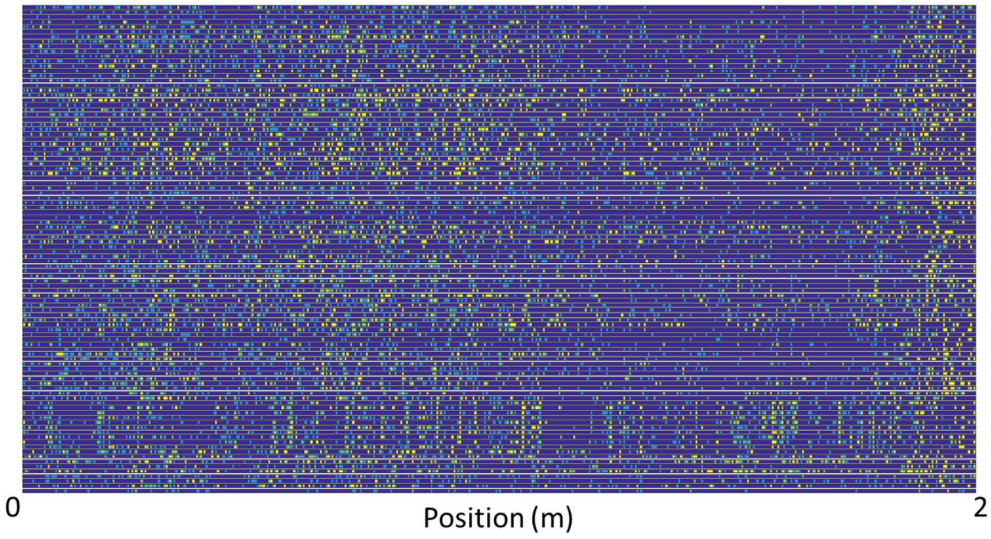

Figure 15. Sample data recorded from the entorhinal cortex. Heat map showing the locations on the virtual track that exhibited increased firing for 100 individual neurons. In each mouse an average of 225 isolatable neurons were recorded from 64 total implanted recording electrodes in the entorhinal cortex.

These data show that mesh electronics are able to record from multiple brain regions while mice are performing a goal-oriented learning task, and that it is possible to observe the putative formation and strengthening of interactions between neurons (**Fig. 16**).

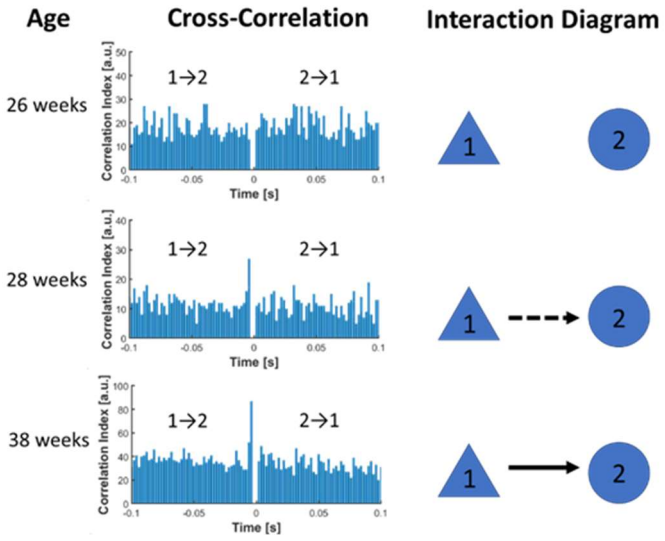

Figure 16. Cross-correlogram between two neurons (left) along with the putative monosynaptic connection diagram (right). These data show the formation and strengthening of an excitatory interaction.

This is an exciting step towards our goal to study time-dependent evolution of neural circuits involved in spatial learning and memory. Next steps will involve more long-term experiments, as well as a thorough evaluation of the massive amount of collected data to understand how the circuit relationship between place cells in the hippocampus and grid cells in the entorhinal cortex corresponds to cognitive performance in the goal-oriented learning tasks.